

# A Polyoxometalate-Based Inorganic Porous Material with both Proton and Electron Conductivity by Light Actuation: Photocatalysis for Baeyer–Villiger Oxidation and Cr(VI) Reduction

Chen Si, Pengtao Ma,\* Qiuxia Han,\* Jiachen Jiao, Wei Du, Jingpin Wu, Mingxue Li, and Jingyang Niu\*

Cite This: *Inorg. Chem.* 2021, 60, 682–691

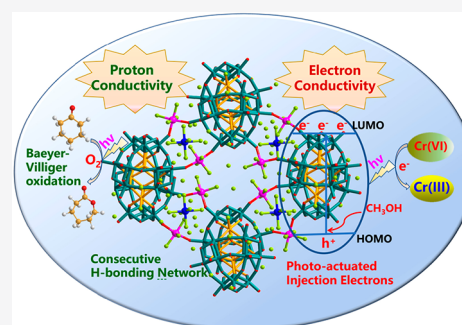
Read Online

ACCESS |

Metrics & More

Article Recommendations

**ABSTRACT:** Two-dimensional (2D) crystalline porous materials with designable structures and high surface areas are currently a hot research topic in the field of proton- and electron-conducting materials, which provide great opportunities to orderly accommodate carriers in available spaces and to accurately understand the conducting path. The 2D dual-conductive inorganic framework  $[\text{Co}(\text{H}_2\text{O})_6]_2\{[\text{Co}(\text{H}_2\text{O})_4]_4[\text{WZn}_3(\text{H}_2\text{O})_2(\text{ZnW}_9\text{O}_{34})_2]\}_2 \cdot 8\text{H}_2\text{O}$  ( $\text{Co}_6\text{Zn}_5\text{W}_{19}$ ) is synthesized by combining  $[\text{WZn}_3(\text{H}_2\text{O})_2(\text{ZnW}_9\text{O}_{34})_2]^{12-}$  ( $\text{Zn}_5\text{W}_{19}$ ) and a Co(II) ion via a hydrothermal method. Due to the presence of a consecutive H-bonding network, electrostatic interactions, and packing effects between the framework and guest molecules,  $\text{Co}_6\text{Zn}_5\text{W}_{19}$  displays a high proton conductivity ( $3.55 \times 10^{-4} \text{ S cm}^{-1}$  under 98% RH and 358 K) by a synergistic effect of the combined components. Additionally, a photoactuated electron injection into the semiconducting materials is an important strategy for switching electronic conductivity, because it can efficiently reduce the frameworks without destroying the crystallinity.  $I-V$  curves of a tablet of  $\text{Co}_6\text{Zn}_5\text{W}_{19}$  in the reduced and oxidized states yield conductivities of  $1.26 \times 10^{-6}$  and  $5 \times 10^{-8} \text{ S cm}^{-1}$ , respectively. Moreover,  $\text{Co}_6\text{Zn}_5\text{W}_{19}$  is also successfully applied in the photocatalytic reduction of the toxic Cr(VI) metal ion by utilizing its excellent electronic storage capacity and Baeyer–Villiger (BV) oxidation in a molecular oxygen/aldehyde system.



## 1. INTRODUCTION

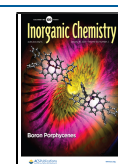
Fuel cells (FCs) can convert chemical energy into electrical energy by carbon-free emission processes, which have become new alternatives to fossil fuels and have attracted much attention owing to their high efficiency and eco-friendly properties.<sup>1,2</sup> In recent years, diverse solid-state proton-/electron-conductive materials have been extensively developed as batteries, chemical sensors, and supercapacitors. Conductive porous crystalline metal–organic frameworks (MOFs) are an emerging class of multidimensional frameworks with high designability and tunability in structure and properties.<sup>3</sup> Especially the high crystallinity and void space of MOFs are beneficial for understanding the conducting path and incorporation of conducting media.<sup>4,5</sup> For example, in 2017, Chen's group reported a structurally flexible and chemically stable MOF, BUT-8(Cr)A, with high proton conductivity in a wide RH range of up to  $1.27 \times 10^{-1} \text{ S cm}^{-1}$  at 80 °C and 100% RH, which possesses hydrophilic pores functionalized by large numbers of  $-\text{SO}_3\text{H}$  sites and a water-content-dependent structural transformation.<sup>6</sup> In 2018, Das' group proposed a simple yet powerful template-assisted strategy for synthesizing the proton-conducting coordination polymers Co-tri, and the proton conduction value reaches  $1.49 \times 10^{-1} \text{ S cm}^{-1}$  under 98% relative humidity and 80 °C.<sup>7</sup> Up to now, five general strategies have been developed for synthesizing proton-

conductive MOFs, such as counterion impregnation, ligand functionalization, metal center functionalization, guest molecule inclusion, and defects in the structure.<sup>2,8</sup> However, most reported conductive MOFs only display a single function, either proton conductivity or electron conductivity.<sup>9</sup> It remains a new challenge to develop a new synthetic strategy for the design of new porous materials with long-range charge delocalization and an H-bonding network, thus endowing them with dual functions of electron and proton conductivity.<sup>10,11</sup>

Polyoxometalates (POMs) are a kind of excellent molecule-based semiconductor with diverse structures, reversible redox activity, and ease of functionalization.<sup>12–14</sup> Especially, POMs are promising charge carriers because they can accept many electrons and protons in multielectron transfer processes without deforming their structures, which is beneficial for applications in heterogeneous photocatalysts and electrochromic or photochromic devices.<sup>15–18</sup> In comparison with

Received: September 4, 2020

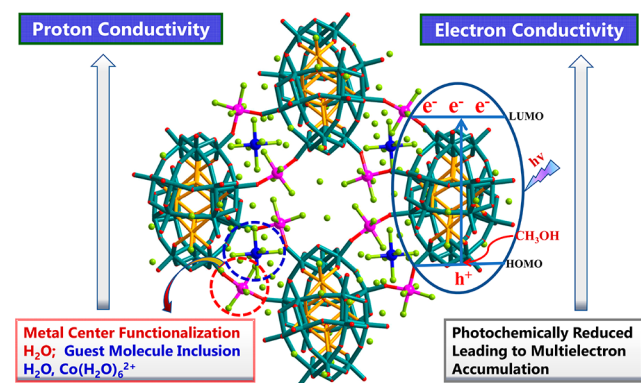
Published: December 23, 2020



the extensively reported POM-based MOFs (POMOFs), pure inorganic frameworks constructed by POMs linking solely with metal bridging units are rare and have recently gained attention as a unique class of materials.<sup>19,20</sup> In 2019, Schimpf's group assembled a new metal oxide material from Preyssler anions  $[\text{NaP}_5\text{W}_{30}\text{O}_{110}]^{14-}$  linked with  $\text{Co}(\text{H}_2\text{O})_4^{2+}$  bridging units, which can be photochemically reduced, allowing the storage of multiple electrons under mild conditions. This addition of delocalized electrons is accompanied by a 1000-fold increase in the conductivity.<sup>21</sup> The sandwich-type POM  $\{\text{Zn}_5\text{W}_{19}\}$  displays incomparable advantages for oxidative catalysis of organic compounds and has been extensively explored. It is worth mentioning that  $\{\text{Zn}_5\text{W}_{19}\}$  has a 0.130 charge/size ratio, which is much higher than that of  $[\text{NaP}_5\text{W}_{30}\text{O}_{110}]^{14-}$  (0.096) (according to the calculation from charge density (charge/atom) = (anionic charge of the POM)/(number of non-hydrogen atoms of the POM)). This peculiar feature makes  $\{\text{Zn}_5\text{W}_{19}\}$  an excellent agent for the recombination of many more metal ions on the surface.<sup>22</sup>

Inspired by this pioneering work, we developed both metal center functionalization and guest molecule inclusion strategies to synthesize the new 2D inorganic framework  $\text{Co}_6\text{Zn}_5\text{W}_{19}$  by assembling Co(II) and high electron density  $\{\text{Zn}_5\text{W}_{19}\}$  via a coordination mode under hydrothermal conditions. In the structure, the Co(II) metal centers are functionalized with  $\text{H}_2\text{O}$ , and free  $\text{Co}(\text{H}_2\text{O})_6^{2+}$  and  $\text{H}_2\text{O}$  are located in the channel as guest molecules (Scheme 1). Due to the presence of a

### Scheme 1. Design Concept for Achieving a Porous Material with Dual Conductivity<sup>a</sup>

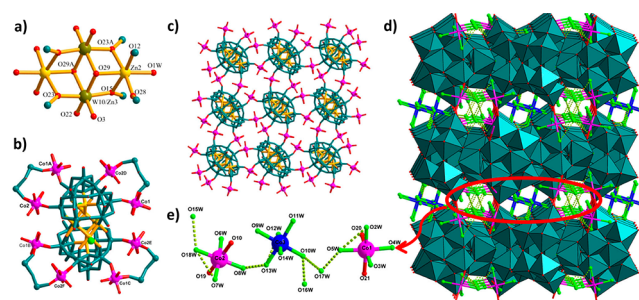


<sup>a</sup>The H-bonding network and photoinduced electron accumulation endow it with proton conductivity and electron conductivity.

consecutive H-bonding network between the framework and guest molecules,  $\text{Co}_6\text{Zn}_5\text{W}_{19}$  displays excellent proton conductivity by a synergistic effect of the combined components.<sup>23,24</sup> Most importantly, this hybrid shows high proton conductivity,  $3.55 \times 10^{-4} \text{ S cm}^{-1}$ , under 98% RH at 358 K. Moreover,  $\text{Co}_6\text{Zn}_5\text{W}_{19}$  gives a high electron conductivity of  $1.26 \times 10^{-6} \text{ S cm}^{-1}$  under the same conditions when it was photochemically reduced by adding  $\text{CH}_3\text{OH}$  as an electron sacrificial reductant, leading to multielectron accumulation.<sup>21</sup> We also explored the photocatalytic reduction of the heavy metal Cr(VI) ion by utilizing its excellent electronic storage capacity. The achievement of dual conductivity in an inorganic framework represents the realization of a general synthetic strategy for the creation of new porous conductor-based devices.<sup>25</sup>

## 2. RESULTS AND DISCUSSION

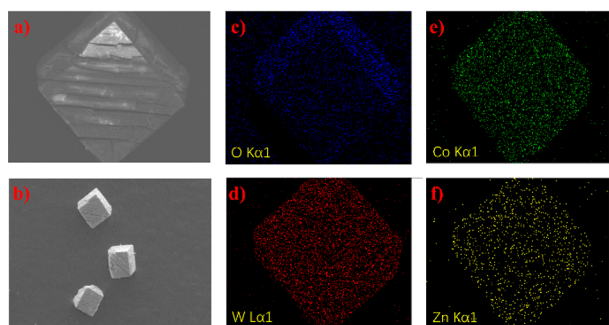
**2.1. Crystal Structure.** A single-crystal X-ray diffraction analysis reveals that  $\text{Co}_6\text{Zn}_5\text{W}_{19}$  crystallizes in the monoclinic  $P2_1/n$  space group. The asymmetric unit of  $\text{Co}_6\text{Zn}_5\text{W}_{19}$  consists of a sandwich-type  $\{\text{Zn}_5\text{W}_{19}\}$  polyoxoanion, two hexacoordinate cobalt cations  $[\text{Co}(\text{H}_2\text{O})_4(\text{O}_t)_2]^{2+}$ , two free  $[\text{Co}(\text{H}_2\text{O})_6]^{2+}$  cations, and eight lattice water molecules.  $\{\text{Zn}_5\text{W}_{19}\}$  contains two trivacant Keggin  $[\text{B-}\alpha\text{-ZnW}_9\text{O}_{34}]^{12-}$  fragments in a staggered fashion linked via a rhomblike  $\text{Zn}_3\text{WO}_{16}$  group in a centrosymmetric arrangement ( $C_{2h}$  symmetry); Zn(3) and W(10) are disordered with 0.5 occupancy. Zn(2) is coordinated with three  $\mu_3\text{-O}$ , two  $\mu_2\text{-O}$ , and one  $\text{Zn-O}_{\text{H}_2\text{O}}$  (Zn-O 2.042(10) Å) (Figure 1a). The



**Figure 1.** (a) Coordination mode of Zn(II) in the belt. (b) Coordination environment of  $\{\text{Zn}_5\text{W}_{19}\}$  unit. (c) Perspective view of the two-dimensional sheet connected by Co(II) ions and  $\{\text{Zn}_5\text{W}_{19}\}$  clusters. (d) 3D H-bonding network of  $\text{Co}_6\text{Zn}_5\text{W}_{19}$  showing the stacking pattern of the gridlike sheets viewed down the  $b$  axis. (e) Consecutive H-bonding mode with  $\text{O}(\text{W})\cdots\text{O}(\text{W})$  distances from 2.40 to 2.90 Å. Free  $[\text{Co}(\text{H}_2\text{O})_6]^{2+}$  is shown in blue, and  $\text{H}_2\text{O}$  molecules are shown in green.

coordination environment of the Zn(2) atom can mimic the active sites of an enzyme to activate molecular oxygen. The  $\{\text{Zn}_5\text{W}_{19}\}$  unit acts as an octagonal ligand to coordinate with eight Co(II) cations via eight terminal oxygen atoms of the belt of eight  $\{\text{WO}_6\}$  octahedra (Figure 1b). The two crystallographically independent Co(II) ions are divided into two categories according to the coordination environment. The Co(1) ion is coordinated in an octahedral geometry with two terminal oxygen atoms and two aqua ligands in the equatorial plane, and two aqua ligand atoms in the axial positions. However, the Co(2) ion is coordinated in an octahedral geometry with four aqua ligands in the equatorial plane, and two terminal oxygen atoms in the axial positions, respectively. The  $\{\text{Zn}_5\text{W}_{19}\}$  moieties are linked by Co(II) cations to form an extended 2D framework (Figure 1c). The 2D sheets further stack to form a 3D network with the accessible pores being about  $564.6 \text{ \AA}^3$  (12.4% void space to accommodate), as calculated from a PLATON analysis.<sup>26</sup> A large amount of free water molecules and  $[\text{Co}(\text{H}_2\text{O})_6]^{2+}$  cations are impregnated in the cavity, as they can tune the hydrophilicity of the pore surface, confer protons, and form hydrogen bonds as the proton migration pathway (Figure 1d). The shorter distances between  $\text{H}_2\text{O}$  molecules vary from 2.4 to 2.9 Å, which verified the strong H-bond formation (Figure 1e). Due to the presence of a consecutive H-bonding network, electrostatic interactions, and packing effects between the framework and guest molecules,  $\text{Co}_6\text{Zn}_5\text{W}_{19}$  displays excellent electron and proton conductivity by a synergistic effect of the combined components.

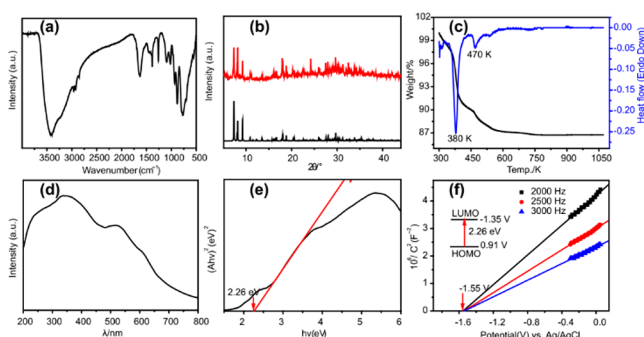
**2.2. Characterizations.** The morphology and structure of  $\text{Co}_6\text{Zn}_5\text{W}_{19}$  were characterized with a scanning electron microscope (SEM) (Figure 2).  $\text{Co}_4\text{Zn}_5\text{W}_{19}$  shows regularly



**Figure 2.** (a, b) Morphology and structure of  $\text{Co}_4\text{Zn}_5\text{W}_{19}$  characterized by SEM. (c–f) EDS elemental mapping images of  $\text{Co}_4\text{Zn}_5\text{W}_{19}$ .

shaped cube blocks. Moreover, energy dispersive spectroscopy (EDS) shows the specific distribution of individual elements in same block of the sample. The different intensities of colors are assumed to be proportional to the metal composition in the same block of the sample.<sup>27</sup> The results show that these elements are homogeneously distributed in the framework of the  $\text{Co}_6\text{Zn}_5\text{W}_{19}$  crystal.

The IR spectra of  $\text{Co}_6\text{Zn}_5\text{W}_{19}$  were collected from solid samples pelletized with KBr in the range of 4000–500  $\text{cm}^{-1}$  (Figure 3a). Figure 3b shows the PXRD patterns of

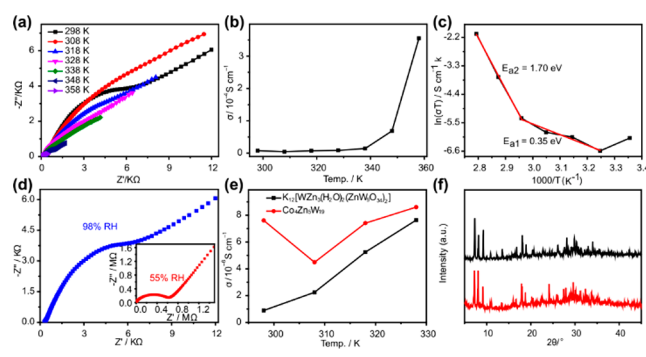


**Figure 3.** Characterizations of  $\text{Co}_6\text{Zn}_5\text{W}_{19}$ : (a) IR spectra; (b) PXRD patterns (bottom, simulated; top, experimental); (c) TG-DTA; (d) solid UV–vis absorption spectrum; (e) Tauc plot; (f) Mott–Schottky plots in 0.1 M  $\text{Na}_2\text{SO}_4$  aqueous solution (the inset gives the energy diagram of the HOMO and LUMO levels of  $\text{Co}_6\text{Zn}_5\text{W}_{19}$ ).

$\text{Co}_6\text{Zn}_5\text{W}_{19}$ . The experimental pattern is well matched with the pattern simulated from single-crystal X-ray diffraction, which confirms the good phase purity of  $\text{Co}_6\text{Zn}_5\text{W}_{19}$ . The strong band at 3421  $\text{cm}^{-1}$  is attributed to the O–H stretching vibration absorption, which verifies the presence of a large amount of crystalline water molecules and H-bonds. The IR spectra also show three very strong absorption peaks near 925 and 876, 769  $\text{cm}^{-1}$  that are assigned to the vibration bands of  $\{\text{Zn}_5\text{W}_{19}\}$ , which is consistent with the result of the X-ray diffraction analysis.<sup>28</sup> The TG curve of  $\text{Co}_6\text{Zn}_5\text{W}_{19}$  indicates one consecutive weight-loss step, which is associated with the loss of lattice water molecules and coordination water molecules with a total loss of 12.3% (calculated 11.5%) (Figure 3c). TGA reveals that the main framework is stable

from 300 to 750 °C, which meets most of the prerequisites as an ideal platform for conductive materials. The UV/vis spectrum of  $\text{Co}_6\text{Zn}_5\text{W}_{19}$  shows very broad absorption throughout the region of 200–800 nm, which demonstrates that it indeed has a good light-harvesting ability (Figure 3d). The adsorption band at 520 nm is ascribed to the  $t_{2g}^6e_g^1 \rightarrow t_{2g}^5e_g^2$  transition of  $[\text{Co}(\text{H}_2\text{O})_6]^{2+}$  cations, which demonstrates that Co has a +2 valence ( $d^7$ ).<sup>29</sup> The strong adsorption at 350 nm is ascribed to  $\text{O}_d \rightarrow \text{W}$  and  $\text{O}_{b,c} \rightarrow \text{W}$  charge transfer absorption bands of  $\{\text{Zn}_5\text{W}_{19}\}$ . Thus, the band gap of  $\text{Co}_6\text{Zn}_5\text{W}_{19}$  is estimated to be 2.26 eV by the Kubelka–Munk (KM) method as described, unveiling its potential to be applied as a semiconducting photocatalyst (Figure 3e). Mott–Schottky measurements indicate that  $\text{Co}_6\text{Zn}_5\text{W}_{19}$  is an n-type semiconductor due to the positive slopes of Mott–Schottky plots. The flat band potential of  $\text{Co}_6\text{Zn}_5\text{W}_{19}$  is estimated to be  $-1.55$  V (vs Ag/AgCl) by the X axis intercept of the linear regions of these plots (Figure 3f). As calculated by the equation  $E_{\text{CB}} = E(\text{vs Ag/AgCl}) + 0.2$  V, the lowest unoccupied molecular orbital (LUMO) value is  $-1.35$  V (vs NHE) for  $\text{Co}_6\text{Zn}_5\text{W}_{19}$ . On the basis of the formula  $E_{\text{VB}} = E_{\text{CB}} + E_g$ , the highest occupied molecular orbital (HOMO) potential value can be calculated as 0.91 V according to the results of UV–vis absorption spectra and electrochemical tests.<sup>30,31</sup>

**2.3. Proton Conductivity Study.** The proton-conducting behavior of  $\text{Co}_6\text{Zn}_5\text{W}_{19}$  was studied by ac impedance measurements under the relative humid environment 98% (RH) and the temperature from 298 to 358 K, and the Nyquist plots are shown in Figure 4a. The arc in the high-frequency



**Figure 4.** Proton conductivity study: (a) impedance spectra under 98% RH conditions at selected temperatures; (b) temperature-dependent proton conductivity; (c) Arrhenius plot of the crystal sample; (d) Nyquist plots of the crystal sample at 98% and 55% RH (inset); (e) proton conductivity comparison between  $\text{Co}_6\text{Zn}_5\text{W}_{19}$  and the precursor; (f) PXRD pattern (top, recycle from proton conductivity; bottom, fresh).

region together with a spike in the low-frequency range is observed at 298 K; these are due to the bulk resistance and electrode contribution, respectively. The proton conductivity is calculated by fitting the arc at selected temperatures using the ZView program, and the temperature dependences of conductivity ( $\sigma$ ) are plotted in both the forms of  $\sigma$  versus  $T$  and  $\ln(\sigma T)$  versus  $1000/T$ . The proton conductivity  $\sigma$  is  $7.61 \times 10^{-6}$   $\text{S cm}^{-1}$  at 298 K, and the value increases with an increase in temperature and reaches  $3.55 \times 10^{-4}$   $\text{S cm}^{-1}$  at 358 K (Table 1). In the temperature region of 298–358 K, as displayed in Figure 4b, one turning point located at 348 K occurs, which is related to the process of losing lattice water. The  $\ln(\sigma T)$  value is plotted against  $1000/T$  in the temperature



**Table 1.** Proton Conductivity for the Oxidized States of  $\text{Co}_6\text{Zn}_5\text{W}_{19}$  at 98% RH and Different Temperatures

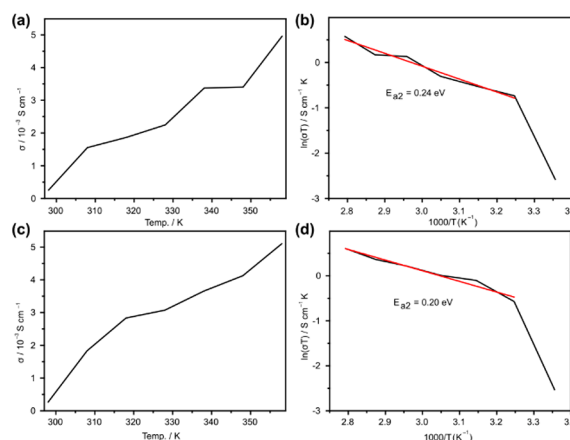
$T$ (K)	$R_p$ ( $\Omega$ )	$\sigma$ ( $\text{S cm}^{-1}$ )
298	17406	$7.61 \times 10^{-6}$
308	29499	$4.49 \times 10^{-6}$
318	17875	$7.41 \times 10^{-6}$
328	15386	$8.61 \times 10^{-6}$
338	9171	$1.44 \times 10^{-5}$
348	1923	$6.89 \times 10^{-5}$
358	372.9	$3.55 \times 10^{-4}$

range of 298–358 K and is shown in Figure 4c. Obviously, the  $\ln(\sigma T)$  versus  $1000/T$  plot shows a nonlinear relationship across the entire temperature range. To roughly estimate the proton transport activation energy  $E_a$ , we fit the temperature-dependent conductivities in two different temperature regions (298–338 and 338–358 K) using the Arrhenius equation,<sup>32</sup> where the corresponding  $\ln(\sigma T)$  vs  $1000/T$  plot shows an approximately linear relationship. The best fits gave the activation energy  $E_{a1} = 0.35$  eV in the range of 308–338 K versus  $E_{a2} = 1.70$  eV in the range of 338–358 K, which correspond to the Grotthuss ( $E_a < 0.4$  eV) and vehicle mechanisms ( $E_a > 0.4$  eV), respectively.<sup>33</sup> The results indicated that the proton-conduction process mainly depends on the temperature, and this is due to the H-bonding network for proton hopping being interrupted when the lattice water molecules were removed with an increase in temperature.

To investigate the relative RH dependences of proton conductance at 298 K for  $\text{Co}_6\text{Zn}_5\text{W}_{19}$ , ac impedance measurements were performed at 55% RH. As expected, it shows a lower conductivity of  $1.40 \times 10^{-7}$  S  $\text{cm}^{-1}$ , where the proton conductivity is strongly affected by the hydration conditions due to the change in H-bonding networks (Figure 4d, inset).<sup>23,24</sup> In comparison, the proton conductivity of the precursor  $\text{K}_{12}[\text{WZn}_3(\text{H}_2\text{O})_3(\text{ZnW}_9\text{O}_{34})_2] \cdot 48\text{H}_2\text{O}$  was also detected from 298 to 328 K at 98% RH (it dissolved at higher temperature), which gave a conductivity of  $8.91 \times 10^{-7}$  S  $\text{cm}^{-1}$  at 298 K and of  $7.64 \times 10^{-6}$  S  $\text{cm}^{-1}$  at 328 K (Figure 4e). The results further demonstrated the good proton transfer ability of POMs.  $\text{Co}_6\text{Zn}_5\text{W}_{19}$  displays a better proton conductivity than the precursor, which can be ascribed to the synergistic effect of the consecutive H-bonding network, electrostatic interactions, and packing effects between the framework and guest molecules.<sup>34,35</sup>

Moreover, when  $\text{Co}_6\text{Zn}_5\text{W}_{19}$  was pretreated in 98% RH for 24 h, it gave a higher proton conductivity of up to  $4.96 \times 10^{-3}$  S  $\text{cm}^{-1}$  at 358 K in comparison to that of the fresh samples (Figure 5). The data of proton conduction in a cycle from 298 to 358 K and then a return from 358 to 298 K verified that the proton conduction is stable (Table 2). The Arrhenius plot of the cycles gave activation energies of 0.24 and 0.20 eV in the range of 308–338 K, respectively, which followed the Grotthuss mechanism. The results further demonstrated that the humidity conditions played a crucial role in the conductivity properties and mechanism. The index of the PXRD pattern of the  $\text{Co}_6\text{Zn}_5\text{W}_{19}$  bulk sample recycled from the proton conduction cycle indicated that its crystallinity was maintained (Figure 4f).

Diverse structures of POMs have been used as excellent proton-conductive materials (Table 3). For example, in 2018, Zhao's group reported an unprecedented giant molecular cerium–bismuth tungstate superstructure formed by self-

**Figure 5.** Experimental data of the proton conduction cycle for the pretreated  $\text{Co}_6\text{Zn}_5\text{W}_{19}$  samples from 298 to 358 K ((a), temperature-dependent proton conductivity; (b), Arrhenius plot) and then a return it from 358 to 298 K ((c), temperature-dependent proton conductivity; (d), Arrhenius plot).**Table 2.** Data of the Proton Conduction Cycle for the Pretreated  $\text{Co}_6\text{Zn}_5\text{W}_{19}$  in 98% RH for 24 h (a) from 298 to 358 K and Then (b) a Return from 358 to 298 K

$T$ (K)	$R_p$ ( $\Omega$ ) <sup>a</sup>	$\sigma$ ( $\text{S cm}^{-1}$ ) <sup>a</sup>	$R_p$ ( $\Omega$ ) <sup>b</sup>	$\sigma$ ( $\text{S cm}^{-1}$ ) <sup>b</sup>
298	1600	$2.55 \times 10^{-4}$	1563	$2.68 \times 10^{-4}$
308	261.8	$1.56 \times 10^{-3}$	222.5	$1.83 \times 10^{-3}$
318	218.3	$1.87 \times 10^{-3}$	143.8	$2.83 \times 10^{-3}$
328	181.3	$2.25 \times 10^{-3}$	132.5	$3.07 \times 10^{-3}$
338	120.8	$3.37 \times 10^{-3}$	111.4	$3.65 \times 10^{-3}$
348	119.7	$3.40 \times 10^{-3}$	98.73	$4.13 \times 10^{-3}$
358	82.2	$4.96 \times 10^{-3}$	79.86	$5.10 \times 10^{-3}$

assembly from simple metal oxide precursors in aqueous solution, which exhibits a good proton conductivity of  $8.3 \times 10^{-4}$  S  $\text{cm}^{-1}$  at 303 K and  $2.6 \times 10^{-4}$  S  $\text{cm}^{-1}$  (50% RH) and  $2.4 \times 10^{-3}$  S  $\text{cm}^{-1}$  (90% RH) at 298 K.<sup>36</sup> In 2019, Lan's group synthesized the new compounds HImMo<sub>132</sub> (Im, imidazole), HMeImMo<sub>132</sub>, ILMo<sub>132</sub>, and TBAMo<sub>132</sub> with hollow structures and HImPMo<sub>12</sub> with a solid spherulike structure. The hollow structure HImMo<sub>132</sub> shows a high proton conductivity of  $4.98 \times 10^{-2}$  S  $\text{cm}^{-1}$  (333 K, 98% RH).<sup>37</sup> In 2017, Li's group developed a facile approach to fabricate bicontinuous polymer nanocomposites through the POM-induced phase transition of lamellar PS-*b*-P2VP. In addition, POMs can act as both high proton conductors and nanoenhancers, endowing the bicontinuous nanocomposites with an increased conductivity of 0.1 mS  $\text{cm}^{-1}$  at room temperature.<sup>38</sup>

**2.4. Electron Conductivity Study.** The unique feature of POMs is their redox activity, which can easily accept many electrons by chemical, photochemical, or electrochemical methods.<sup>21</sup> Photoinduced electron injection into POMs is an important strategy for switching electronic conductivity, because it can efficiently reduce the frameworks without destroying the crystallinity. High electron conductivity was simultaneously achieved with the pure protonic nature of the  $\text{Co}_6\text{Zn}_5\text{W}_{19}$  due to the addition of excess electrons to the semiconducting material. The reduced  $\text{Co}_6\text{Zn}_5\text{W}_{19}$  framework ( $\text{R-Co}_6\text{Zn}_5\text{W}_{19}$ ) was acquired by above-gap illumination in the presence of the sacrificial reductant MeOH using a 365 nm LED for 6 h, leading to a large amount of electron accumulation in the metal oxide. Here, MeOH was oxidized

Table 3. Comparison of Proton Conductivities in Some Reported POM-Incorporated Compounds

material	$\sigma$ (S cm <sup>-1</sup> )	RH (%), T (K)	ref
HPW@MIL-101	$1.5 \times 10^{-2}$	100, 353	5
K <sub>11.1</sub> H <sub>2.9</sub> [Na(H <sub>2</sub> O)P <sub>5</sub> W <sub>30</sub> O <sub>110</sub> ] $\cdot$ 0.3PEG400 $\cdot$ 28H <sub>2</sub> O	$2.5 \times 10^{-4}$	<10, 368	22
K <sub>11.9</sub> H <sub>2.1</sub> [Na(H <sub>2</sub> O)P <sub>5</sub> W <sub>30</sub> O <sub>110</sub> ] $\cdot$ 0.2PEG1000 $\cdot$ 26H <sub>2</sub> O	$1.7 \times 10^{-4}$	<10, 368	22
K <sub>13.0</sub> H <sub>1.0</sub> [Na(H <sub>2</sub> O)P <sub>5</sub> W <sub>30</sub> O <sub>110</sub> ] $\cdot$ 0.03PAA5000 $\cdot$ 20H <sub>2</sub> O	$1.7 \times 10^{-3}$	75, 338	22
K <sub>10.2</sub> H <sub>1.8</sub> [Bi(H <sub>2</sub> O)P <sub>5</sub> W <sub>30</sub> O <sub>110</sub> ] $\cdot$ 3.6PEG400 $\cdot$ 11H <sub>2</sub> O	$4.0 \times 10^{-4}$	<10, 368	22
{[Na(NO <sub>3</sub> )(H <sub>2</sub> O)] <sub>4</sub> [Al <sub>16</sub> (OH) <sub>24</sub> (H <sub>2</sub> O) <sub>8</sub> (P <sub>8</sub> W <sub>48</sub> O <sub>184</sub> )] <sup>16-</sup>	$4.5 \times 10^{-2}$	70, 358	23
Co <sub>1.5</sub> (C <sub>4</sub> H <sub>6</sub> N <sub>3</sub> O) <sub>3</sub> [P <sub>2</sub> Mo <sub>5</sub> O <sub>23</sub> ] $\cdot$ 8.5H <sub>2</sub> O	$3.6 \times 10^{-4}$	97, 371	34
(POM) <sub>10</sub> - <i>b</i> -poly(COOH) <sub>300</sub>	0.053	100, 298	36
PMoV2@MIL-101	$6.3 \times 10^{-3}$	~98, 353	37
PMoV2@MIL-101/PVA/PVP	$2.0 \times 10^{-3}$	~98, 353	38

to formaldehyde and concomitantly delivered 2e<sup>-</sup> and 2H<sup>+</sup> to the metal oxide. Several delocalized electrons in the POM can be repeated to accumulate by the photochemical reaction and are stable indefinitely when kept anaerobic. Figure 6 shows the

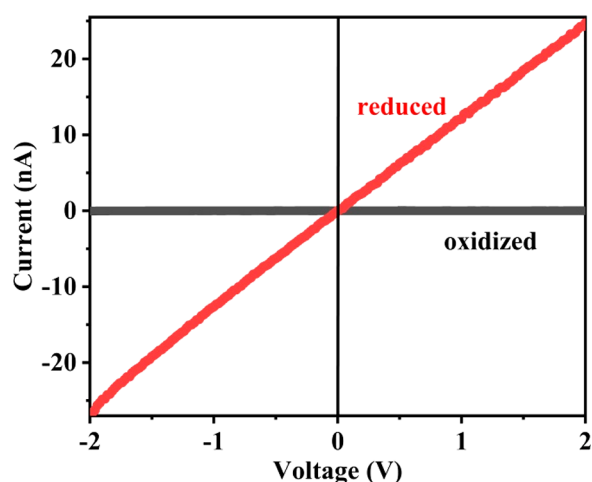


Figure 6. *I*–*V* curves of the tablet of Co<sub>6</sub>Zn<sub>5</sub>W<sub>19</sub> in the reduced (red line) and oxidized (black line) states. The conductivities were determined to be  $1.26 \times 10^{-6}$  and  $5 \times 10^{-8}$  S cm<sup>-1</sup> for the reduced and oxidized states, respectively.

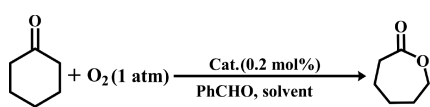
*I*–*V* curves of the tablet of Co<sub>6</sub>Zn<sub>5</sub>W<sub>19</sub> in the reduced (red) and oxidized (black) states. Linear fits to the data yield conductivities of  $1.26 \times 10^{-6}$  and  $5 \times 10^{-8}$  S cm<sup>-1</sup> for the reduced and oxidized states, respectively.

**2.5. Catalysis.** **2.5.1. Photocatalytic Baeyer–Villiger Oxidation.** The Baeyer–Villiger (BV) oxidation is a powerful method to synthesize important intermediates in the chemical, polymers, and drug industries by converting ketones into the corresponding esters or lactones. Initially, persulfate in concentrated sulfuric acid and other strong oxidants such as perbenzoic acid, *m*-chloroperbenzoic acid (*m*-CPBA), and H<sub>2</sub>O<sub>2</sub> activated by Lewis acids were widely used in the classical BV reaction.<sup>39,40</sup> The disadvantages of instability, shock sensitivity, and potential explosiveness in transport and storage seriously restricted its development. Therefore, the direct utilization of O<sub>2</sub> as the primary oxidant in the BV oxidation under mild conditions has recently attained widespread interest as a promising technology for green molecular transformations. Metal complexes, such as Cu(OAc)<sub>2</sub>, Ni(OAc)<sub>2</sub>, Ni(oxa)<sub>2</sub>, Co(acac)<sub>2</sub>, and Fe(TPP)Cl, have been applied to this catalytic system.<sup>41</sup> Meanwhile, Mukaiyama et al. disclosed that aerobic BV oxidation can be achieved through the in situ generation of organic peroxyacids via the joint use of

O<sub>2</sub> and aldehydes catalyzed by nickel(II) complexes coordinated with 1,3-diketones.<sup>42</sup> However, the reported homogeneous catalytic systems have limitations in the complicated synthesis process, inferior chemoselectivity, and difficult separation of the catalyst/product, and the low catalytic activity needs further strengthening. Therefore, it is necessary to develop a simple and feasible strategy to synthesize heterogeneous catalysts for BV oxidation with O<sub>2</sub>.

Recently, the applications of {Zn<sub>5</sub>W<sub>19</sub>} have mainly concentrated on oxidation catalysis. For example, Neumann's group first applied {Zn<sub>5</sub>W<sub>19</sub>} as an efficient homogeneous catalyst to the selective oxidation of various functional groups with H<sub>2</sub>O<sub>2</sub>. Moreover, transition-metal-substituted POMs showed better catalytic performance for activating O<sub>2</sub> in comparison to their parents, due to tuning of the electronic structure and high stability of the redox states.<sup>43</sup> In 2017, Wu's group reported the new porous POM framework CZJ-11 combining Cu-substituted POMs {Zn<sub>3</sub>Cu<sub>2</sub>W<sub>19</sub>} and Gd(III) anions for highly efficient biomimetic aerobic oxidation of aliphatic alcohols with molecular oxygen as a homogeneous catalyst.<sup>44</sup> Assembling the Lewis acid catalyst Co(II) and reversible redox activity catalyst {Zn<sub>5</sub>W<sub>19</sub>} into an inorganic framework via coordination mode would be an effective approach to achieve the synergy of the multiple catalytic sites for efficient electron transfer, high activity, and good stability.

The BV oxidation of cyclohexanone (2 mmol) with O<sub>2</sub> (1 atm) and aldehyde was initially examined along with Co<sub>6</sub>Zn<sub>5</sub>W<sub>19</sub> (0.2% mol ratio) in 1,2-dichloromethane (DCM) by a single workup stage at 50 °C for 12 h. The results are given in Table 4. Cyclohexanone as a model reaction only gave  $\epsilon$ -caprolactone in 26.8% yield (Table 4, entry 1). Subsequently, the optimization of reaction conditions was investigated. First, we detected the effect of solvents by selecting different solvents such as 1,2-dichloroethane (DCE), MeCN, and EtOAc instead of DCM. In DCE, a higher conversion with ideal yield (57.0%) was obtained in comparison to MeCN and EtOAc (Table 4, entries 2–4). The effect of solvents can be attributed to the excellent electrochemical stability of DCE. Benzaldehyde as the sacrificial reductant was also important to the reaction. Furthermore, the effect of varying the benzaldehyde loading was examined. The ratio of cyclohexanone and PhCHO was modified from 1/2 to 2/1. A decrease in benzaldehyde loading afforded a poor  $\epsilon$ -caprolactone yield of 39.2% (Table 4, entry 5). When the ratio was raised to 1/2, the yield of the reaction increased to 99.6% (Table 4, entry 6). These results verified benzaldehyde as the sacrificial reductant was very important to the reaction. An increase in reaction temperature also results in an increased yield (Table 4, entries 7–9). The reaction gave an

**Table 4. Optimization of the Baeyer–Villiger Oxidation Reaction Conditions<sup>a</sup>**


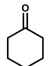
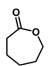
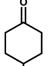
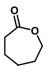
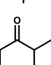
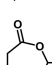
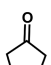
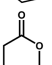
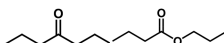
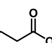
entry	solvent	sub/PhCHO	yield (%) <sup>b</sup>
1	DCM	1/1	26.8
2	MeCN	1/1	42.2
3	EtOAc	1/1	41.0
4	DCE	1/1	57.0
5 <sup>c</sup>	DCE	2/1	39.2
6	DCE	1/2	96.8
7 <sup>d</sup>	DCE	1/2	36.1
8 <sup>e</sup>	DCE	1/2	90.1
9 <sup>f</sup>	DCE	1/2	4.1

<sup>a</sup>Reaction conditions unless specified otherwise: cyclohexanone (2.0 mmol), PhCHO, O<sub>2</sub> (1 atm), catalyst (0.2 mol %), and solvent (5 mL) at 50 °C for 12 h. <sup>b</sup>The calculation of yields was based on GC-MS measurements. <sup>c</sup>The ratio based on the substrate. <sup>d</sup>Reaction at 25 °C. <sup>e</sup>Reaction at 70 °C. <sup>f</sup>Reaction under an N<sub>2</sub> atmosphere.

excellent yield of  $\epsilon$ -caprolactone (96.8%) at 50 °C. When the reaction temperature was increased to 70 °C, the yield of  $\epsilon$ -caprolactone slightly decreased to 90.1%. When the reaction was performed under a nitrogen atmosphere, the yield was decreased to only 5%, proving that O<sub>2</sub> as an oxidant is vital to the reaction. Co<sub>6</sub>Zn<sub>5</sub>W<sub>19</sub> shows high activity as a heterogeneous catalyst in the BV oxidation of cyclic ketones, which provides effective evidence for our initial design.

Utilizing the optimized reaction conditions, the oxidation of various ketones was run to further ascertain the scope of the present method (Table 5). 4-Methylcyclohexanone was

**Table 5. BV Oxidation of Various Ketones<sup>a</sup>**

Entry	Subs	Products	T(h)	Yield(%) <sup>[b]</sup>
1			12	96.8
2			16	99.1
3			16	98.8
4			16	82.7
5			16	trace

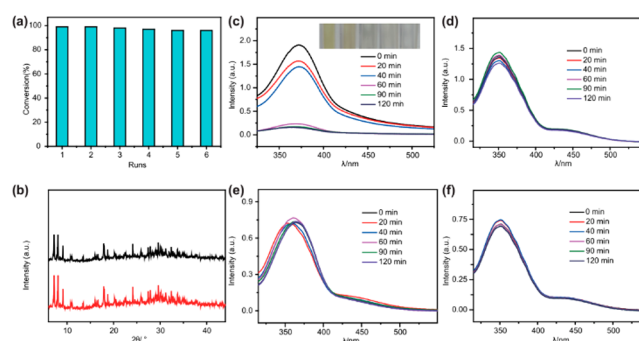
<sup>a</sup>Reactions were conducted on a 2.0 mmol scale in 5 mL of DCE in a round-bottom flask with an O<sub>2</sub> balloon. <sup>b</sup>Conversion, selectivity, and yields were calculated by GC measurements based on the internal standard method.

converted into the corresponding 4-methyl- $\epsilon$ -caprolactone in 99.1% yield in 16 h (Table 5, entry 2). Similarly, 2-methylcyclohexanone as the substrate was added to the reaction system, which rearranged regioselectively to give 6-methyl- $\epsilon$ -caprolactone in 98.8% yield (Table 5, entry 3). The reaction of cyclopentanone still proceeded smoothly to form

BV products in an 82.7% yield after the reaction time was increased to 16 h (Table 5, entry 2). As expected, the aliphatic ketone 4-heptanone exhibited a poor yield with under the same reaction conditions because of its large chemical steric hindrance and high energy of the transition state in comparison with those of cyclic ketones. Both the stereochemistry and reactivity are consistent with other reports of BV oxidation.

To further investigate the catalytic properties of Co<sub>6</sub>Zn<sub>5</sub>W<sub>19</sub>, we set up a series of control experiments. Cyclohexanone was selected as the reaction substrate. First, the oxidation of cyclohexanone under the optimized reaction conditions in the absence of Co<sub>6</sub>Zn<sub>5</sub>W<sub>19</sub> generated 2.6%  $\epsilon$ -caprolactone. When {Zn<sub>5</sub>W<sub>19</sub>} was simply added to the reaction system, there was a yield of 74.5%. The increase in yield in comparison to the absence of catalyst indicated that {Zn<sub>5</sub>W<sub>19</sub>} was effective in catalyzing the oxidation of benzaldehyde to the corresponding carboxylic acid. Then, a loading of 0.4% mol of Co(NO<sub>3</sub>)<sub>2</sub> further improved the yield to 88.6%. These results confirmed that {Zn<sub>5</sub>W<sub>19</sub>} and the Lewis acid site Co<sup>II</sup> synergistically catalyze the oxidation of the ketones.

To verify the nature of the heterogeneous catalysis of Co<sub>6</sub>Zn<sub>5</sub>W<sub>19</sub>, it was removed via centrifugal separation from the reaction mixture of cyclohexanone after 6 h, and the filtrate did not yield extra BV products under identical reaction conditions after being stirred at 50 °C for another 6 h. Solids of Co<sub>6</sub>Zn<sub>5</sub>W<sub>19</sub> could be isolated from the reaction suspension by simple filtration alone and reused at least six times with a moderate loss of activity (from 96% to 90% of yield for  $\epsilon$ -caprolactone) (Figure 7a). The index of the PXRD pattern of



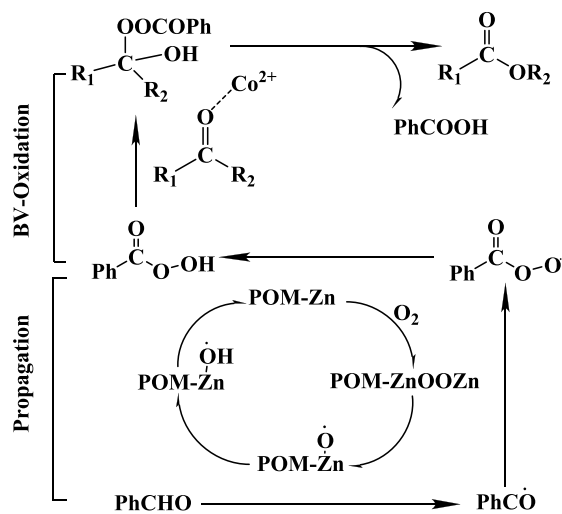
**Figure 7.** (a) Recyclability tests of the Co<sub>6</sub>Zn<sub>5</sub>W<sub>19</sub> catalyst for the photocatalytic BV oxidation. (b) PXRD pattern (top, recycle from proton conductivity; bottom, fresh). Photocatalytic reduction of Cr(VI): (c) with Co<sub>6</sub>Zn<sub>5</sub>W<sub>19</sub> as the catalyst after different times of visible light irradiation (inset: pictures of the Cr(VI) solutions at different reaction time under visible light); (d) without MeOH; (e) with the precursor K<sub>12</sub>[WZn<sub>3</sub>(H<sub>2</sub>O)<sub>3</sub>(ZnW<sub>9</sub>O<sub>34</sub>)<sub>2</sub>]·48H<sub>2</sub>O as the catalyst; (f) without light.

the Co<sub>6</sub>Zn<sub>5</sub>W<sub>19</sub> bulky sample recycled from catalytic reaction indicated that the crystallinity was maintained. These observations proved the heterogeneous catalytic nature of Co<sub>6</sub>Zn<sub>5</sub>W<sub>19</sub> (Figure 7b).

On the basis of the results of our study and the enzyme catalysts already reported, a possible mechanism is illustrated in Scheme 2. First, Zn(II) as the transition-metal-substituted sites activates molecular oxygen to accomplish the O–O bond heterolysis, forming a highly reactive metal–oxo species as the active oxidant. Hydrogen at the  $\alpha$ -carbon position of benzaldehyde was abstracted by metal–oxo species to obtain



**Scheme 2. Proposed Mechanism for the Oxygen/Aldehyde/Polyoxometalate System Catalyst in Baeyer–Villiger (BV) Oxidation**



acyl radicals, which provide the main way to obtain acyl radicals in comparison with the autoxidation of aldehydes. Acyl radicals combine subsequently with  $O_2$  to form acylperoxy radical intermediates, which convert to peroxybenzoic acid by consumption of benzaldehyde. Subsequently, the formation of  $\epsilon$ -caprolactones can be drawn from the reaction between the forming peroxybenzoic acid and cyclohexanone via the Criegee adduct. Another main pathway was carried out:  $Co^{II}$  activated the carbonyl as the Lewis acid sites with peracid to also form the “Criegee adduct intermediates”, which further rearrange to obtain the Baeyer–Villiger product.

**2.5.2. Photoreduction of Cr(VI).** The hexavalent chromium anion  $Cr(VI)$  is one of the most toxic heavy-metal contaminants, which severely threaten the environment and human health. Therefore, rapid and efficient detection and reduction of trace  $Cr(VI)$  anions in water are particularly urgent.<sup>45,46</sup> Owing to the excellent electronic storage capacity of  $Co_6Zn_5W_{19}$ , it was explored in the photocatalytic reduction for the heavy-metal  $Cr(VI)$  ion with visible light irradiation. A solution of  $0.5 \text{ mmol L}^{-1} K_2Cr_2O_7$  with  $CH_3OH$  as an electron sacrificial reductant was irradiated by a 10 W white led lamp for 90 min, indicating the almost complete reduction of  $Cr(VI)$  (Figure 7c). Notably, the reduction process increased dramatically after irradiation for 40 min, which may benefit from the electron accumulation with time. The control experiments indicated that the reduction of  $Cr(VI)$  is almost inert in the absence of light, methanol, or catalyst  $Co_6Zn_5W_{19}$  (Figure 7d–f). Even when the precursor  $K_{12}[WZn_3(H_2O)_3(ZnW_9O_{34})_2] \cdot 48H_2O$  was employed as a catalyst, the reduction efficiency was also negligible. The great performance of  $Co_6Zn_5W_{19}$  should be ascribed to the photoactuated electron injection into the semiconducting materials, which is vital for the reduction process. Herein, a possible photocatalytic mechanism of  $Co_6Zn_5W_{19}$  is provided. When  $Co_6Zn_5W_{19}$  is above-gap irradiated in the presence of the sacrificial reductant  $CH_3OH$ , a large number of delocalization electrons were generated and concomitantly  $2H^+$  was delivered, which favors the progress of  $Cr(VI)$  reduction. On the basis of Mott–Schottky measurements, the  $E_{CB}(LUMO)$  positions are more negative than the reduction potentials of  $Cr(VI)/Cr(III)$  to many products (0.51 eV vs

NHE); it is theoretically feasible to use  $Co_6Zn_5W_{19}$  as a catalyst for  $Cr_2O_7^{2-}$  for photoreduction.<sup>47</sup>

### 3. CONCLUSION

In conclusion, the interesting inorganic porous material  $Co_6Zn_5W_{19}$  was successfully synthesized by utilizing a new synthetic strategy that combined the redox POM and  $Co(II)$  ions. It possesses long-range charge delocalization and H-bonding network, thus endowing it with electron and proton conductivity simultaneously.  $Co_6Zn_5W_{19}$  displays a high proton conductivity ( $3.55 \times 10^{-4} \text{ S cm}^{-1}$  under 98% RH and 358 K) by a synergistic effect of the combined components. The best fits gave the activation energy  $E_{a1} = 0.35 \text{ eV}$  in the range of 298–338 K versus  $E_{a2} = 1.70 \text{ eV}$  in the range of 338–358 K, which correspond to the Grotthuss ( $E_a < 0.4 \text{ eV}$ ) and vehicle mechanisms ( $E_a > 0.4 \text{ eV}$ ), respectively. Overall, the strategies of metal center functionalization and guest molecule inclusion in the 2D materials could be an effective way to improve the proton conductivity. Additionally, excellent electron conductivity is also achieved by the redox-switchable behavior of the POMs. Moreover,  $Co_6Zn_5W_{19}$  displayed high efficiency in the photocatalytic reduction of the toxic metal  $Cr(VI)$  ion by utilizing its excellent electronic storage capacity.

### 4. EXPERIMENTAL SECTION/METHODS

**4.1. Materials and Methods.** All chemicals and reagents used in this study were reagent grade and were used without further purification.  $K_{12}[WZn_3(H_2O)_3(ZnW_9O_{34})_2] \cdot 48H_2O$  was synthesized according to the literature.<sup>48</sup> The elemental analyses (EA) of C, H, and N were performed on a Vario EL III elemental analyzer. The inductively coupled plasma (ICP) spectroscopic analyses of Zn, Co, and W were performed on a Jarrel-Ash Model J-A1100 spectrometer. IR spectra were collected from the powder sample with KBr pellets as the base on a JASCO FT/IR-430 spectrometer. Thermogravimetric analysis was carried out on a Mettler-Toledo TGA/SDTA 851e instrument heated from 25 to 800 °C with a heating rate of  $10 \text{ }^\circ\text{C min}^{-1}$ , under a dynamic nitrogen atmosphere. The diffuse reflectance UV–vis absorption spectra were obtained on a Hitachi UH4150 spectrophotometer (Japan). The morphology of the sample was characterized by using a Zeiss MERLIN field-emission scanning electron microscope (SEM). Mott–Schottky measurements were carried out on a CHI 760E electrochemical workstation (Shanghai Chenhua Instrument Co., China) in a three-electrode electrochemical cell using  $0.1 \text{ M Na}_2\text{SO}_4$  as the electrolyte. Impedance data were collected under anhydrous conditions using Solartron 1260 and 1296 impedance phase gain analyzers, and the scanning frequencies ranged from 10 MHz to 0.01 Hz, with a voltage of 0.1 V. The  $I$ – $V$  curve test was constructed with a Keithley 2400 source meter, a xenon light source, a probe station, and a computer equipped with measurement software. The photocatalytic reactions were performed on WATT-CAS Parallel Light Reactor (WP-TEC-1020HSL) with a 10 W COB LED.

**4.2. Preparation of  $Co_6Zn_5W_{19}$ .**  $Co_6Zn_5W_{19}$  was prepared under hydrothermal conditions by a self-assembly approach.  $Co(NO_3)_2 \cdot 3H_2O$  (60.0 mg, 0.20 mmol) and  $K_{12}[WZn_3(H_2O)_3(ZnW_9O_{34})_2] \cdot 48H_2O$  (50 mg, 0.01 mmol) were dissolved in 6.0 mL of mixed solution of water (4.0 mL) and methanol (2.0 mL), and the resultant mixture was stirred over 12 h. The resulting suspension was sealed in a 25 mL Teflon-lined reactor and kept at 120 °C for 4 days. After the autoclave was cooled to room temperature, pink rhombus single crystals were separated, washed with water, and air-dried (yield: ca. 72%). Anal. Calcd for  $H_7Co_6O_{106}W_{19}Zn_5$ : Co, 5.95; Zn, 5.50; W, 58.74. Found: Co, 5.99; Zn, 5.46; W, 58.64.

**4.3. Single-Crystal X-ray Crystallography.** A good single crystal of  $Co_6Zn_5W_{19}$  with dimensions of  $0.15 \times 0.11 \times 0.08 \text{ mm}^3$  was prudentially picked under an optical microscope and sealed in a

glass tube closed at both ends. Intensity data were collected on a Bruker APEX-II CCD detector at 296(2) K with Mo K $\alpha$  radiation ( $\lambda = 0.71073$  Å). Using Olex2, the structure was solved with the olex2.solve structure solution program using charge flipping and refined with the olex2.refinement package using Gauss–Newton minimization.<sup>49,50</sup> All H atoms on water molecules were directly included in the molecular formula. A summary of crystal data and structure refinement details for Co<sub>6</sub>Zn<sub>5</sub>W<sub>19</sub> is provided in Table 6.

**Table 6. Crystal Data and Structure Refinement Details for Co<sub>6</sub>Zn<sub>5</sub>W<sub>19</sub>**

empirical formula	H <sub>76</sub> Co <sub>6</sub> O <sub>106</sub> W <sub>19</sub> Zn <sub>5</sub>
formula wt	5946.19
cryst syst	monoclinic
space group	P2 <sub>1</sub> /n
a (Å)	15.3518(12)
b (Å)	19.0781(14)
c (Å)	15.5436(12)
$\beta$ (deg)	91.2080(10)
V (Å <sup>3</sup> )	4551.4(6)
calcd density (Mg m <sup>-3</sup> )	4.283
Z	2
abs coeff (mm <sup>-1</sup> )	26.374
F(000)	5132
$\theta$ (deg)	2.132–25.098
hkl range	$-18 \leq h \leq 17, -22 \leq k \leq 22,$ $-18 \leq l \leq 10$
no. of collected/unique reflns	23536/8103 (R(int) = 0.0522)
GOF	1.043
R1 <sup>a</sup> ( $I > 2\sigma(I)$ )	0.0402
wR2 <sup>b</sup> ( $I > 2\sigma(I)$ )	0.0834
R1 <sup>a</sup> (all data)	0.0534
wR2 <sup>b</sup> (all data)	0.0885
diff peak/hole (e Å <sup>-3</sup> )	1.93/–2.12

<sup>a</sup>R1 =  $\sum ||F_o| - |F_c|| / \sum |F_o|$ , <sup>b</sup>wR2 =  $[\sum w(F_o^2 - F_c^2)^2 / \sum w(F_o^2)^2]^{1/2}$ ,  $w = 1/[\sigma^2(F_o^2) + (xP)^2 + yP]$ , and  $P = (F_o^2 + 2F_c^2)/3$ , where  $x = 0.0298$  and  $y = 64.6200$  for Co<sub>6</sub>Zn<sub>5</sub>W<sub>19</sub>.

**4.4. Proton Conductivity.** The fresh crystal samples were compressed into 5 mm diameter tablets at a pressure of 0.5 MPa, with a thickness of about 0.026 cm. The pretreated Co<sub>6</sub>Zn<sub>5</sub>W<sub>19</sub> sample at 98% RH for 24 h has a thickness of about 0.08 cm. Impedance data were collected under different humidity condition using Solartron 1260 and 1296 impedance phase gain analyzers, and the scanning frequencies ranged from 10 MHz to 0.01 Hz with a voltage of 0.1 V. The conductivity test was performed under the test conditions with a relative humidity (RH) of 98% and a temperature interval of 298–358 K (25–85 °C). The measurements were carried out for 2 h at each testing temperature. The conductivity ( $\sigma$ ) was calculated using the equation  $\sigma = L/RS$ , where  $L$  is the sample thickness,  $S$  is the cross-sectional area, and  $R$  represents the resistance.

**4.5. Electron Conductivity.** The fresh crystal samples were compressed into 5 mm diameter tablets at a pressure of 0.5 MPa, with a thickness of about 0.03 cm. The tablet was placed in a probe station. The oxidized Co<sub>6</sub>Zn<sub>5</sub>W<sub>19</sub> was first measured by two conductive electrodes. Then the reduced Co<sub>6</sub>Zn<sub>5</sub>W<sub>19</sub> framework was obtained by above-gap illumination in the presence of the sacrificial reductant MeOH using a 365 nm LED for 6 h, leading to a great amount of electron accumulation in the metal oxide, and measured.

**4.6. Photocatalytic Baeyer–Villiger Oxidation.** The BV oxidation reaction was carried out in a three-necked flask, 2 mmol of ketone as the substrate, 4 mmol of benzaldehyde as the co-oxidant, and a 0.2 mol % catalytic amount of Co<sub>6</sub>Zn<sub>5</sub>W<sub>19</sub>, and 1,2-dichloroethane (5 mL) was added as the solvent. Then 1 atm of oxygen was supplied by a balloon as the oxygen source, in the closed device. The reaction mixture was heated to 50 °C, and the reaction

was stopped after stirring for 8 h. After reaction for the desired time, the catalyst was filtered, and the final mixture was filtered and evaporated under reduced pressure to give the product. The conversion and selectivity were determined by a GS-MS analysis (Agilent 8860) of the final solution after the reaction.

**4.7. Photocatalytic Cr(VI) Reduction.** Potassium dichromate (K<sub>2</sub>Cr<sub>2</sub>O<sub>7</sub>) was selected as the Cr(VI) source for photocatalytic testing in visible light. The specific operation was as follows: 5 mg of Co<sub>6</sub>Zn<sub>5</sub>W<sub>19</sub> was dispersed in 2.5 mL of a Cr(VI) aqueous solution and 2.5 mL of CH<sub>3</sub>OH, and then the mixed solution was exposed to 10 W white light. After different irradiation times, the solution was removed from the suspension and the catalyst was removed by centrifugation for analysis. The photocatalytic process of the compound was studied by UV–vis absorption spectroscopy.

## ■ ASSOCIATED CONTENT

### Accession Codes

CCDC 1909642 contains the supplementary crystallographic data for this paper. These data can be obtained free of charge via [www.ccdc.cam.ac.uk/data\\_request/cif](http://www.ccdc.cam.ac.uk/data_request/cif), or by emailing [data\\_request@ccdc.cam.ac.uk](mailto:data_request@ccdc.cam.ac.uk), or by contacting The Cambridge Crystallographic Data Centre, 12 Union Road, Cambridge CB2 1EZ, UK; fax: +44 1223 336033.

## ■ AUTHOR INFORMATION

### Corresponding Authors

**Pengtao Ma** – Henan Key Laboratory of Polyoxometalate Chemistry, Institute of Molecular and Crystal Engineering, School of Chemistry and Chemical Engineering, Henan University, Kaifeng 475004, People's Republic of China; [orcid.org/0000-0002-0587-8635](https://orcid.org/0000-0002-0587-8635); Email: [mpt@henu.edu.cn](mailto:mpt@henu.edu.cn)

**Qixia Han** – Henan Key Laboratory of Polyoxometalate Chemistry, Institute of Molecular and Crystal Engineering, School of Chemistry and Chemical Engineering, Henan University, Kaifeng 475004, People's Republic of China; [orcid.org/0000-0002-0175-562X](https://orcid.org/0000-0002-0175-562X); Email: [hdhqx@henu.edu.cn](mailto:hdhqx@henu.edu.cn)

**Jingyang Niu** – Henan Key Laboratory of Polyoxometalate Chemistry, Institute of Molecular and Crystal Engineering, School of Chemistry and Chemical Engineering, Henan University, Kaifeng 475004, People's Republic of China; [orcid.org/0000-0001-6526-7767](https://orcid.org/0000-0001-6526-7767); Email: [jyniu@henu.edu.cn](mailto:jyniu@henu.edu.cn)

### Authors

**Chen Si** – Henan Key Laboratory of Polyoxometalate Chemistry, Institute of Molecular and Crystal Engineering, School of Chemistry and Chemical Engineering, Henan University, Kaifeng 475004, People's Republic of China

**Jiachen Jiao** – Henan Key Laboratory of Polyoxometalate Chemistry, Institute of Molecular and Crystal Engineering, School of Chemistry and Chemical Engineering, Henan University, Kaifeng 475004, People's Republic of China

**Wei Du** – Henan Key Laboratory of Polyoxometalate Chemistry, Institute of Molecular and Crystal Engineering, School of Chemistry and Chemical Engineering, Henan University, Kaifeng 475004, People's Republic of China

**Jingpin Wu** – Henan Key Laboratory of Polyoxometalate Chemistry, Institute of Molecular and Crystal Engineering, School of Chemistry and Chemical Engineering, Henan University, Kaifeng 475004, People's Republic of China

**Mingxue Li** – Henan Key Laboratory of Polyoxometalate Chemistry, Institute of Molecular and Crystal Engineering,



School of Chemistry and Chemical Engineering, Henan University, Kaifeng 475004, People's Republic of China;  
✉ [orcid.org/0000-0003-2760-2020](https://orcid.org/0000-0003-2760-2020)

Complete contact information is available at:  
<https://pubs.acs.org/10.1021/acs.inorgchem.0c02658>

## Notes

The authors declare no competing financial interest.

## ACKNOWLEDGMENTS

This work was supported by the National Natural Science Foundation of China (grant nos. 22071043 and 21601048), the Key Scientific Research Project of Henan Higher Education Institutions (grant no. 20ZX006), the Natural Science Foundation of Henan (grant no. 202300410043), and the Henan University First-class Discipline Cultivation Project (grant no. 2019YLZDJL10).

## REFERENCES

- (1) Meng, X.; Wang, H. N.; Song, S. Y.; Zhang, H. J. Proton-Conducting Crystalline Porous Materials. *Chem. Soc. Rev.* **2017**, *46* (2), 464–480.
- (2) Lim, D. W.; Kitagawa, H. Proton Transport in Metal-Organic Frameworks. *Chem. Rev.* **2020**, *120* (16), 8416–8467.
- (3) Luo, H. B.; Wang, M.; Liu, S. X.; Xue, C.; Tian, Z. F.; Zou, Y.; Ren, X. M. Proton Conductance of a Superior Water-Stable Metal-Organic Framework and Its Composite Membrane with Poly(vinylidene Fluoride). *Inorg. Chem.* **2017**, *56* (7), 4169–4175.
- (4) Wang, M.; Luo, H. B.; Zhang, J.; Liu, S. X.; Xue, C.; Zou, Y.; Ren, X. M. An Open-Framework Manganese(II) Phosphite and its Composite Membranes with Polyvinylidene Fluoride Exhibiting Intrinsic Water-Assisted Proton Conductance. *Dalton. T.* **2017**, *46* (24), 7904–7910.
- (5) Lai, X.; Liu, Y.; Yang, G.; Liu, S.; Shi, Z.; Lu, Y.; Luo, F.; Liu, S. Controllable Proton-Conducting Pathways via Situating Polyoxometalates in Targeting Pores of a Metal-Organic Framework. *J. Mater. Chem. A* **2017**, *5* (20), 9611–9617.
- (6) Yang, F.; Xu, G.; Dou, Y.; Wang, B.; Zhang, H.; Wu, H.; Zhou, W.; Li, J.-R.; Chen, B. A Flexible Metal-organic Framework with a High Density of Sulfonic Acid Sites for Proton Conduction. *Nat. Energy.* **2017**, *2* (11), 877–883.
- (7) Elahi, S. M.; Chand, S.; Deng, W.; Pal, A.; Das, M. C. Polycarboxylate-Templated Coordination Polymers: Role of Templates for Superprotonic Conductivities of up to  $10^{-1}$  S Cm<sup>-1</sup>. *Angew. Chem., Int. Ed.* **2018**, *57* (22), 6662–6666.
- (8) Cao, J.; Ma, W.; Lyu, K.; Zhuang, L.; Cong, H.; Deng, H. Twist and Sliding Dynamics between Interpenetrated Frames in Ti-MOF Revealing High Proton Conductivity. *Chem. Sci.* **2020**, *11* (15), 3978–3985.
- (9) Chen, T.; Dou, J. H.; Yang, L.; Sun, C.; Libretto, N. J.; Skorupskii, G.; Miller, J. T.; Dincă, M. Continuous Electrical Conductivity Variation in M<sub>3</sub>(Hexaiminotriphenylene)<sub>2</sub> (M = Co, Ni, Cu) MOF Alloys. *J. Am. Chem. Soc.* **2020**, *142* (28), 12367–12373.
- (10) Mendes, R. F.; Barbosa, P.; Domingues, E. M.; Silva, P.; Figueiredo, F.; Almeida Paz, F. A. Enhanced Proton Conductivity in a Layered Coordination Polymer. *Chem. Sci.* **2020**, *11* (24), 6305–6311.
- (11) Luo, H. B.; Wang, M.; Zhang, J.; Tian, Z. F.; Zou, Y.; Ren, X. M. Open-Framework Chalcogenide Showing both Intrinsic Anhydrous and Water-Assisted High Proton Conductivity. *ACS Appl. Mater. Interfaces* **2018**, *10* (3), 2619–2627.
- (12) Shi, Z.; Li, J.; Han, Q.; Shi, X.; Si, C.; Niu, G.; Ma, P.; Li, M. Polyoxometalate-Supported Aminocatalyst for the Photocatalytic Direct Synthesis of Imines from Alkenes and Amines. *Inorg. Chem.* **2019**, *58* (19), 12529–12533.
- (13) Lin, J.; Li, N.; Yang, S.; Jia, M.; Liu, J.; Li, X. M.; An, L.; Tian, Q.; Dong, L. Z.; Lan, Y. Q. Self-Assembly of Giant Mo<sub>240</sub>Hollow Opening Dodecahedra. *J. Am. Chem. Soc.* **2020**, *142* (32), 13982–13988.
- (14) Cao, X.; Wang, Y.; Lin, J.; Ding, Y. Ultrathin CoO<sub>x</sub> Nanolayers Derived from Polyoxometalate for Enhanced Photoelectrochemical Performance of Hematite Photoanodes. *J. Mater. Chem. A* **2019**, *7* (11), 6294–6303.
- (15) He, J.; Li, J.; Han, Q.; Si, C.; Niu, G.; Li, M.; Wang, J.; Niu, J. Photoactive Metal-Organic Framework for the Reduction of Aryl Halides by the Synergistic Effect of Consecutive Photoinduced Electron-Transfer and Hydrogen-Atom-Transfer Processes. *ACS Appl. Mater. Interfaces* **2020**, *12* (2), 2199–2206.
- (16) Zhang, D.; Zhang, W.; Lin, Z.; Dong, J.; Zhen, N.; Chi, Y.; Hu, C. Mono- and Di-Sc-Substituted Keggin Polyoxometalates: Effective Lewis Acid Catalysts for Nerve Agent Simulant Hydrolysis and Mechanistic Insights. *Inorg. Chem.* **2020**, *59* (14), 9756–9764.
- (17) Chen, X.; Zhou, Y.; Roy, V. A. L.; Han, S. Evolutionary Metal Oxide Clusters for Novel Applications: Toward High-Density Data Storage in Nonvolatile Memories. *Adv. Mater.* **2018**, *30* (3), 1703950.
- (18) Lee, C.; Jeon, D.; Park, J.; Lee, W.; Park, J.; Kang, S. J.; Kim, Y.; Ryu, J. Tetra-ruthenium Polyoxometalate as an Atom-Efficient Bifunctional Oxygen Evolution Reaction/Oxygen Reduction Reaction Catalyst and Its Application in Seawater Batteries. *ACS Appl. Mater. Interfaces* **2020**, *12* (29), 32689–32697.
- (19) Xing, S.; Han, Q.; Shi, Z.; Wang, S.; Yang, P.; Wu, Q.; Li, M. A Hydrophilic Inorganic Framework Based on a Sandwich Polyoxometalate: Unusual Chemoselectivity for Aldehydes/ketones with in Situ Generated Hydroxylamine. *Dalton. T.* **2017**, *46* (35), 11537–11541.
- (20) Chang, W.; Qi, B.; Song, Y. F. Step-by-Step Assembly of 2D Confined Chiral Space Endowing Achiral Clusters with Asymmetric Catalytic Activity for Epoxidation of Allylic Alcohols. *ACS Appl. Mater. Interfaces* **2020**, *12* (32), 36389–36397.
- (21) Turo, M. J.; Chen, L.; Moore, C. E.; Schimpf, A. M. Co<sup>2+</sup> Linked [NaP<sub>5</sub>W<sub>30</sub>O<sub>110</sub>]<sup>14-</sup>: A Redox-Active Metal Oxide Framework with High Electron Density. *J. Am. Chem. Soc.* **2019**, *141* (11), 4553–4557.
- (22) Zhang, T.; Liu, S.; Kurth, D. G.; Faul, C. F. J. Organized Nanostructured Complexes of Polyoxometalates and Surfactants That Exhibit Photoluminescence and Electrochromism. *Adv. Funct. Mater.* **2009**, *19* (4), 642–652.
- (23) Yang, P.; Alsufyani, M.; Emwas, A.; Chen, C.; Khashab, N. M. Lewis Acid Guests in a {P<sub>8</sub>W<sub>48</sub>} Archetypal Polyoxotungstate Host: Enhanced Proton Conductivity via Metal-Oxo Cluster within Cluster Assemblies. *Angew. Chem., Int. Ed.* **2018**, *57* (40), 13046–13051.
- (24) Chand, S.; Elahi, S. M.; Pal, A.; Das, M. C. Metal-Organic Frameworks and Other Crystalline Materials for Ultrahigh Superprotonic Conductivities of 10<sup>-2</sup> S Cm<sup>-1</sup> or Higher. *Chem. - Eur. J.* **2019**, *25* (25), 6259–6269.
- (25) Qiao, X. Q.; Zhang, Z. W.; Li, Q. H.; Hou, D.; Zhang, Q.; Zhang, J.; Li, D. S.; Feng, P.; Bu, X. In Situ Synthesis of n-n Bi<sub>2</sub>MoO<sub>6</sub> & Bi<sub>2</sub>S<sub>3</sub> Heterojunctions for Highly Efficient Photocatalytic Removal of Cr(VI)<sup>†</sup>. *J. Mater. Chem. A* **2018**, *6* (45), 22580–22589.
- (26) Spek, A. L. Single-crystal Structure Validation with the Program PLATON. *J. Appl. Crystallogr.* **2003**, *36*, 7–13.
- (27) Shi, Z.; Niu, G.; Han, Q.; Shi, X.; Li, M. A Molybdate-Incorporated Cooperative Catalyst: High Efficiency in the Assisted Tandem Catalytic Synthesis of Cyclic Carbonates from CO<sub>2</sub> and Olefins. *Mol. Catal.* **2018**, *461*, 10–18.
- (28) Dhifallah, F.; Belkhiria, M. S.; Parent, L.; Leclerc, N.; Cadot, E. A Series of Octahedral First-Row Transition-Metal Ion Complexes Templated by Wells-Dawson Polyoxometalates: Synthesis, Crystal Structure, Spectroscopic, and Thermal Characterizations, and Electrochemical Properties. *Inorg. Chem.* **2018**, *57* (19), 11909–11919.
- (29) Kovala-Demertzi, D.; Hadjipavlou-Litina, D.; Staninska, M.; Primikiri, A.; Kotoglou, C.; Demertzis, M. A. Anti-Oxidant, in Vitro, in Vivo anti-Inflammatory Activity and Antiproliferative Activity of Mefenamic Acid and Its Metal Complexes with manganese(II),

cobalt(II), nickel(II), copper(II) and zinc(II). *J. Enzyme Inhib. Med. Chem.* **2009**, *24* (3), 742–752.

(30) Yang, G.; Liang, Y.; Li, K.; Yang, J.; Xu, R.; Xie, X. Construction of a Ce<sup>3+</sup> Doped CeO<sub>2</sub>/Bi<sub>2</sub>MoO<sub>6</sub> Heterojunction with a Mutual Component Activation System for Highly Enhancing the Visible-light Photocatalytic Activity for Removal of TC or Cr(VI)<sup>†</sup>. *Inorg. Chem. Front.* **2019**, *6* (6), 1507–1517.

(31) Wang, X. K.; Liu, J.; Zhang, L.; Dong, L. Z.; Li, S. L.; Kan, Y. H.; Li, D. S.; Lan, Y. Q. Monometallic Catalytic Models Hosted in Stable Metal-Organic Frameworks for Tunable CO<sub>2</sub> Photoreduction. *ACS Catal.* **2019**, *9* (3), 1726–1732.

(32) Zhao, H. R.; Xue, C.; Li, C. P.; Zhang, K. M.; Luo, H. B.; Liu, S. X.; Ren, X. M. A Two-Dimensional Inorganic-Organic Hybrid Solid of Manganese(II) Hydrogenophosphate Showing High Proton Conductivity at Room Temperature. *Inorg. Chem.* **2016**, *55* (17), 8971–8975.

(33) Su, J.; He, W.; Li, X. M.; Sun, L.; Wang, H. Y.; Lan, Y. Q.; Ding, M.; Zuo, J. L. High Electrical Conductivity in a 2D MOF with Intrinsic Superprotonic Conduction and Interfacial Pseudo-Capacitance. *Matter.* **2020**, *2* (3), 711–722.

(34) Cao, X. L.; Xie, S. L.; Li, S. L.; Dong, L. Z.; Liu, J.; Liu, X. X.; Wang, W. B.; Su, Z. M.; Guan, W.; Lan, Y. Q. A Well-Established POM-Based Single-Crystal Proton-Conducting Model Incorporating Multiple Weak Interactions. *Chem. - Eur. J.* **2018**, *24* (10), 2365–2369.

(35) Luo, H. B.; Ren, L. T.; Ning, W. H.; Liu, S. X.; Liu, J. L.; Ren, X. M. Robust Crystalline Hybrid Solid with Multiple Channels Showing High Anhydrous Proton Conductivity and a Wide Performance Temperature Range. *Adv. Mater.* **2016**, *28* (8), 1663–1667.

(36) Liu, J. C.; Han, Q.; Chen, L. J.; Zhao, J. W.; Streb, C.; Song, Y. F. Aggregation of Giant Cerium-Bismuth Tungstate Clusters into a 3D Porous Framework with High Proton Conductivity. *Angew. Chem., Int. Ed.* **2018**, *57* (28), 8416–8420.

(37) Liu, W. J.; Dong, L. Z.; Li, R. H.; Chen, Y. J.; Sun, S. N.; Li, S. L.; Lan, Y. Q. Different Protonic Species Affecting Proton Conductivity in Hollow Spherulike Polyoxometalates. *ACS Appl. Mater. Interfaces* **2019**, *11* (7), 7030–7036.

(38) Zhang, L.; Cui, T.; Cao, X.; Zhao, C.; Chen, Q.; Wu, L.; Li, H. Inorganic-Macroion-Induced Formation of Bicontinuous Block Copolymer Nanocomposites with Enhanced Conductivity and Modulus. *Angew. Chem., Int. Ed.* **2017**, *56* (31), 9013–9017.

(39) Leisch, H.; Morley, K.; Lau, P. C. K. Baeyer-Villiger Monooxygenases: More Than Just Green Chemistry. *Chem. Rev.* **2011**, *111* (7), 4165–4222.

(40) Gao, D.; Jin, F.; Lee, J. K.; Zare, R. N. Aqueous Microdroplets Containing Only Ketones or Aldehydes Undergo Dakin and Baeyer-Villiger Reactions. *Chem. Sci.* **2019**, *10* (48), 10974–10978.

(41) Wang, J.; Zhai, Y.; Wang, Y.; Yu, H.; Zhao, W.; Wei, Y. Selective Aerobic Oxidation of Halides and Amines with an Inorganic-Ligand Supported Zinc Catalyst. *Dalton. T.* **2018**, *47* (38), 13323–13327.

(42) Yamada, T.; Takahashi, K.; Kato, K.; Takai, T.; Inoki, S.; Mukaiyama, T. The Baeyer-Villiger Oxidation of Ketones Catalyzed by Nickel(II) Complexes with Combined Use of Molecular Oxygen and an Aldehyde. *Chem. Lett.* **1991**, *20*, 641–644.

(43) Weinstock, I. A.; Schreiber, R. E.; Neumann, R. Dioxygen in Polyoxometalate Mediated Reactions. *Chem. Rev.* **2018**, *118* (5), 2680–2717.

(44) Zhao, M.; Zhang, X. W.; Wu, C. D. Structural Transformation of Porous Polyoxometalate Frameworks and Highly Efficient Biomimetic Aerobic Oxidation of Aliphatic Alcohols. *ACS Catal.* **2017**, *7* (10), 6573–6580.

(45) Zhang, L.; Li, P.; Feng, L.; Chen, X.; Jiang, J.; Zhang, S.; Zhang, A.; Chen, G.; Wang, H. Controllable Fabrication of Visible-Light-Driven CoS<sub>x</sub>/CdS Photocatalysts with Direct Z-Scheme Heterojunctions for Photocatalytic Cr(VI) Reduction with High Efficiency. *Chem. Eng. J.* **2020**, *397*, 125464.

(46) Gong, Y.; Hu, Q.; Guo, Y.; Yu, L. Photocatalyzed Reduction of Chromium(VI) and Thermal-Driven Heterogeneous Separation. *ACS Sustainable Chem. Eng.* **2017**, *5* (6), 4511–4516.

(47) Niu, G.; Si, C.; Jiao, J.; Han, Q.; Guo, M.; Li, M. An Electron-Rich Metal-Organic Framework for Highly Efficient Photocatalytic Reduction of Cr(VI). *J. Alloys Compd.* **2020**, *830*, 154696.

(48) Tourne, C. M.; Tourne, G. F.; Zonneville, F. Chiral Polytungstometalates [WM<sub>3</sub>(H<sub>2</sub>O)<sub>2</sub>(XW<sub>9</sub>O<sub>34</sub>)<sub>2</sub>]<sup>2-</sup> (X = M = Zn or Co) and their M-Substituted Derivatives. Syntheses, Chemical, Structural and Spectroscopic Study of Some D, L Sodium and Potassium Salts. *J. Chem. Soc., Dalton Trans.* **1991**, 143–155.

(49) Dolomanov, O. V.; Bourhis, L. J.; Gildea, R. J.; Howard, J. A. K.; Puschmann, H. OLEX2: A Complete Structure Solution, Refinement and Analysis Program. *J. Appl. Crystallogr.* **2009**, *42* (2), 339–341.

(50) Bourhis, L. J.; Dolomanov, O. V.; Gildea, R. J.; Howard, J. A. K.; Puschmann, H. *Acta Crystallogr., Sect. A: Found. Adv.* **2015**, *A71*, 59–75.